AAS 21-681

CONVERGENCE BASIN ANALYSIS FOR SPACECRAFT TRAJECTORY TARGETING

Collin E. York[*], Kathleen C. Howell[†], and Belinda Marchand[‡]

One robustness measure in trajectory targeting is the ability to determine feasible trajectories under dispersions. If sufficiently large dispersions cannot be accommodated, unpredictable targeting behavior may result. Dynamical properties of the reference path and the targeting problem formulation influence the region of perturbations for which a targeting strategy reliably produces a feasible reference trajectory, denoted the convergence basin. Characterization of this basin is explored in the Circular Restricted Three-Body Problem and a higher-fidelity model. A basin metric produced from 1st- and 2nd-order state transition tensors evaluated on the reference path is introduced, and the correlation with discretized approaches is summarized.

INTRODUCTION

One measure for assessing targeting robustness in spaceflight applications is the ability of a targeting scheme to determine a feasible trajectory in the presence of dispersions. If the mission trajectory and targeter cannot accommodate sufficiently large dispersions, the result is unpredictable targeting behavior and, potentially, a failure to converge on an acceptable solution or, perhaps, any solution at all. Thus, this investigation is focused on the identification of sensitive trajectories and the development of robust references. The objective of this effort is characterization of the region that defines state perturbations for which a targeting strategy will reliably correct a perturbed trajectory to a feasible reference. This region in perturbation space, denoted the *convergence basin*, is determined by an interaction between the dynamical properties of the baseline or reference path and the selection of the targeting scheme, including the constraint, design variables, and update formulation. In this investigation, characterization of the convergence basin is explored in the Circular Restricted Three-Body Problem (CRTBP) as well as an ephemeris force model. Frequently, sensitivity to perturbations is assessed through simulating the targeting process for a set of discrete points in the perturbation space. Yet, this discretized approach is computationally intensive, requiring multiple numerically-integrated predictions and matrix inversion calculations. This investigation introduces a basin metric produced from 1st- and 2nd-order state transition tensors evaluated solely on the reference path. The correlation with discretized approaches is then summarized.

Previous investigators have explored the characterization and then the improvement of convergence behavior for corrections schemes based on Newton-Raphson approaches. Epitropakis and

[*]Ph.D. Student, School of Aeronautics and Astronautics, Purdue University, 701 W. Stadium Avenue, West Lafayette, IN 47907; york0@purdue.edu

[†]Hsu Lo Distinguished Professor of Aeronautics and Astronautics, School of Aeronautics and Astronautics, Purdue University, 701 W. Stadium Avenue, West Lafayette, IN 47907; howell@purdue.edu

[‡]Adjunct Associate Professor, Purdue University, Austin, TX, 78754; marchand@purdue.edu

Vrahatis applied Newton's method, as well as alternative strategies, to the determination of regions of attraction for periodic orbits in nonlinear systems.[1] Harden and Spreen applied finite-time Lyapunov exponents (FTLEs) to node, or patch point, placement in a Two-Level Targeter (TLT) strategy within the CRTBP and ephemeris force models, respectively.[2,3] Additionally, Spreen investigated the use of state transition tensors above 1st-order in calculating FTLE values across arcs within a targeting problem.[3,4] Then, FTLE values are also applied as weightings in the minimum norm update computation to improve the convergence behavior of the TLT.[5] By assuming that trajectory segments possessing a large magnitude of dynamical stretching correspond to a reduction in the validity of the linear corrections process, these investigations demonstrate improvements in the convergence behavior of the targeting algorithm. Muralidharan's investigation into robust station-keeping algorithms utilizes both the magnitude and direction of dynamical stretching through analysis of the Cauchy-Green tensor.[6,7] The methodology in this investigation seeks to expand on these results by measuring the convergence basin directly and correlating this measurement with the dynamical properties of the reference.

DYNAMICAL MODELS

To mirror applications of targeting problems in both preliminary and later stages of mission design, a characterization of the convergence basins is introduced under two different dynamical models, one associated with the CRTBP and one with higher-fidelity ephemerides for gravitational bodies. By exploring convergence basin prediction under differing dynamical conditions, this investigation examines broader applicability of the methods.

Circular Restricted Three-Body Problem

Many contemporary space flight missions, such as those within the Artemis program,[8,9] employ the CRTBP for the preliminary design and analysis of the trajectories. The CRTBP provides a dynamical model for the motion of a spacecraft under the significant influence of two primary gravitational bodies, P_1 and P_2, where P_1 arbitrarily corresponds to the primary body with the largest mass.[10] A simplifying assumption that the two primaries move in circular orbits about their mutual barycenter is applied and the spacecraft is assumed to possess negligible mass. These assumptions produce a framework for the motion of a spacecraft in the Earth-Moon system.

Insights into the dynamics emerge when the system is viewed from a reference frame centered at the barycenter and rotating with the primary system. The unit vector $\hat{\boldsymbol{x}}$ is defined in the direction from P_1 to P_2, and the unit vector $\hat{\boldsymbol{z}}$ is in the direction of the orbital angular momentum of the primary system. The unit vector $\hat{\boldsymbol{y}}$ completes the triad as $\hat{\boldsymbol{z}} \times \hat{\boldsymbol{x}}$. The characteristic quantities in the primary system include (*i*) the distance between the primaries for length, (*ii*) the time required for the primary system to rotate by one radian in an inertial frame for time, and (*iii*) the sum of the masses of the primary bodies for mass. The mass parameter, μ, is defined as the mass of P_2 divided by the sum of the primaries' masses. Let $\boldsymbol{\rho}$ be the nondimensional position vector from the barycenter to the spacecraft. Then, the nondimensional equations of motion are expressed as

$$\ddot{\boldsymbol{\rho}} = \begin{bmatrix} \ddot{x} \\ \ddot{y} \\ \ddot{z} \end{bmatrix} = \begin{bmatrix} 2\dot{y} + x - \frac{(1-\mu)(x+\mu)}{d^3} - \frac{\mu(x-1+\mu)}{r^3} \\ -2\dot{x} + y - \frac{(1-\mu)y}{d^3} - \frac{\mu y}{r^3} \\ -\frac{(1-\mu)z}{d^3} - \frac{\mu z}{r^3} \end{bmatrix} \tag{1}$$

where d and r represent the nondimensional distances between the spacecraft and the primaries, P_1 and P_2, respectively.

The $\mathcal{N}$-Body Problem

At later stages in the mission design process, trajectories are transitioned to a higher-fidelity dynamical model, incorporating the ephemerides of the gravitational bodies of interest. In this investigation, spacecraft motion is numerical integrated in the J2000 inertial reference frame using the Adaptive Trajectory Design (ATD) software tool[11] developed at Purdue University; NASA's Navigation and Ancillary Information Facility SPICE toolkit is incorporated for planetary ephemeris data. The motion of the spacecraft, body q, with respect to the central body i is determined via gravitational interactions with perturbing bodies j, i.e.,

$$\ddot{\boldsymbol{r}}_{qi} = -G\frac{(m_i + m_q)}{r_{qi}^3}\boldsymbol{r}_{qi} + G\sum_{\substack{j=1 \\ j\neq i,q}} m_j\left(\frac{\boldsymbol{r}_{ij}}{r_{ij}^3} - \frac{\boldsymbol{r}_{qj}}{r_{qj}^3}\right) \tag{2}$$

where G is the gravitational constant. In this investigation, the mass of the spacecraft is assumed to be negligible while the Earth, Moon, and Sun are incorporated and approximated as point-masses.

CONVERGENCE BASIN ANALYSIS

To frame the analysis, suppose a *baseline*, or *reference*, trajectory is known to satisfy a set of constraints. Such a baseline trajectory might be a periodic orbit, a transfer path, an intermediate leg, or even a complex combination of these elements. Typically, this baseline trajectory is the solution to a prior differential corrections or constrained optimization problem. In an operational spacecraft targeting or guidance scenario, the reference might be a baseline path, designed prior to launch, for which considerable analysis has been conducted. In flight, as the spacecraft deviates from the path due to perturbing forces and stochastic sources of error, the baseline is no longer viable, and an updated feasible path is required. The effects of these deviations are modeled as state perturbations applied to the baseline trajectory. A targeting scheme is required to produce a new solution in the vicinity of the reference that retains the important characteristics of the baseline solution while satisfying the imposed set of constraints.

Background

If a perturbation is applied to a baseline solution, the resulting perturbed trajectory, in general, does not satisfy the imposed constraints. The *perturbation variables*, states altered relative to the baseline solution, e.g., inertial position at the initial time or a velocity component, are represented by the vector $\boldsymbol{\mathcal{Y}}$. The perturbation itself, $\delta\boldsymbol{\mathcal{Y}}$, is applied to the baseline, and a targeter is employed to re-converge on a feasible solution within k_{max} iterations via a Newton-Raphson corrections process. To target a new feasible solution nearby the baseline, the iterative differential corrections process incorporates an update to a *design variable* vector, $\boldsymbol{\mathcal{X}}$, to produce a constraint vector, $\boldsymbol{F}(\boldsymbol{\mathcal{X}}, \boldsymbol{\mathcal{Y}})$, that is ideally equal to $\mathbf{0}$. The states that constitute the design variables may or may not also exist as perturbation variables. For a targeting problem with an equal number of constraints and design variables, this correction step via a 1st-order Newton-Raphson update is expressed as

$$\delta\boldsymbol{\mathcal{X}} = -\frac{\partial\boldsymbol{F}}{\partial\boldsymbol{\mathcal{X}}}\bigg|^{-1}_{(\boldsymbol{\mathcal{X}},\boldsymbol{\mathcal{Y}})}\boldsymbol{F}\big|_{(\boldsymbol{\mathcal{X}},\boldsymbol{\mathcal{Y}})} \tag{3}$$

where the design variable Jacobian, $\frac{\partial\boldsymbol{F}}{\partial\boldsymbol{\mathcal{X}}}$, and the constraint vector are evaluated for the design and perturbation variable vector pairs $(\boldsymbol{\mathcal{X}}, \boldsymbol{\mathcal{Y}})$. Since the Newton-Raphson method computes an update

to the design variables based on a linear approximation of a nonlinear system, multiple iterations are required to converge the constraints to within some tolerance.

The convergence basin, or *basin of attraction*, for a solution to the iterative Newton-Raphson problem is defined as the region in perturbation space for which initial guesses converge to that specific solution. For problems where more than one solution exists globally, a local convergence basin exists for each solution. Recall that the true solutions are likely unknown for nonlinear problems and are determined to within an error tolerance. In the field of mathematics, the convergence basin and its properties are studied within the application of root-finding algorithms.[1] Methods exist for determining local regions for which a Newton-Raphson corrections problem converges at particular rates, e.g., quadratically or superlinearly; however, these approaches require analysis of derivatives continuously across the region of perturbation space.[12] In the dynamical systems of interest to this investigation, this analysis is not possible, so the exact regions for which the Newton-Raphson process will converge at a particular rate cannot be exactly determined. At the boundaries of these main basins, the convergence behavior becomes more complex. For polynomial root-finding algorithms in the complex plane, these boundaries between main basins form intricate fractal patterns.[1,13] In trajectory targeting applications, the boundaries between main basins are characteristically chaotic, resulting in unpredictable convergence to an arbitrary local solution or, possibly, no convergence within a reasonable number of iterations. Thus, a characterization of the main basin associated with a baseline solution is necessary if convergence in the presence of perturbations must be guaranteed.

A main basin of convergence for a sample baseline solution is illustrated on a planar perturbation space in Figure 1 to visualize the structure and define a framework for its characterization. The

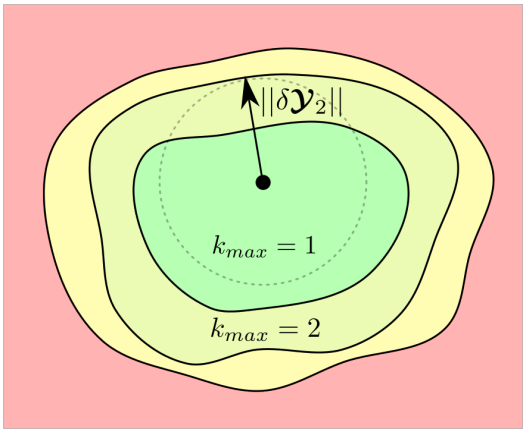

Figure 1. Idealized Basin Width

reference solution is represented by the black point, and the colored contours reflect theoretical continuous convergence basin regions for various iteration limits, k_{max}. As the contours shift from green to yellow, more iterations are required to converge from the perturbed trajectory to a feasible solution in the vicinity of the reference. The red area represents the chaotic region bounding the main basin where convergence behavior is unpredictable. The convergence basin width, $||\delta\boldsymbol{\mathcal{Y}}_{k_{max}}||$, for each limit of k_{max} iterations is defined as the maximum radius of a sphere in perturbation space, originating from the baseline solution, for which all points in the region converge to the baseline within the iteration limit. In Figure 1, the construction of the defining sphere and the convergence basin width are illustrated for a 2-iteration limit. At some point, increasing the iteration

limit, k_{max}, ceases to yield meaningful results as the behavior transitions to chaos. Ideally, the exact basin width is determined by continuously traversing the perturbation space; however, this approach is numerically impossible. Therefore, alternative methods for approximating the basin width are necessary. Three basin width approximation methods are explored in this analysis: naïve perturbation space discretization, principal direction search, and 2nd order sensitivity evaluation for the reference.

Discretized Targeting Simulations

Since the convergence basins cannot be determined analytically, numerical methods are required to approximate the basins. A naïve discretization perturbation space is the closest to approximating a continuous search across the perturbation space, assuming that the points are sufficiently refined. This discretization of the full perturbation space may be structured as a regularized grid search or a randomly-sampled Monte Carlo analysis. However, this approach is the most computationally expensive, because a full targeting simulation is required at each discretized point. In Figure 2(a), a schematic representation of this regularized grid search strategy is overlayed on the illustrative convergence basin from Figure 1. The regularly-spaced points are colored according to the number of

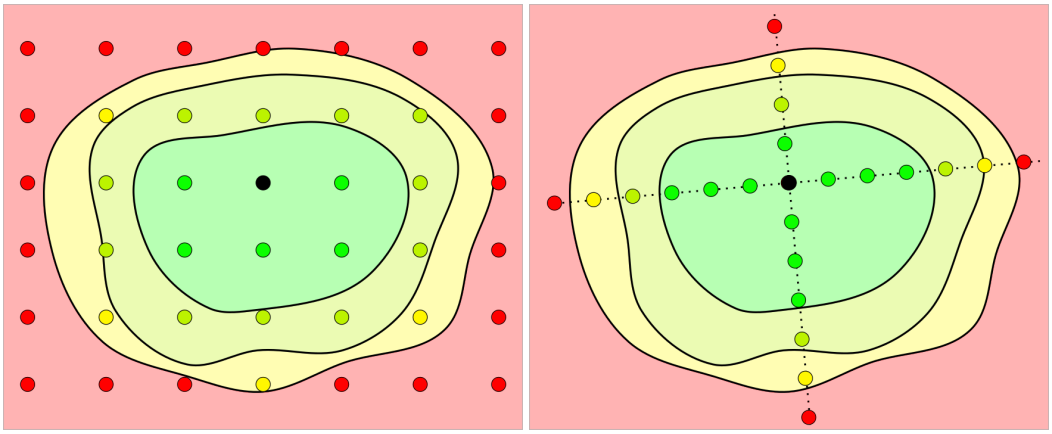

(a) Naïve Discretization (b) Principal Direction Search

Figure 2. Discretization Methods

iterations required for convergence, demonstrating that the naïve discrete method seeks to represent the underlying contours through an array of numerous targeting simulations. To recover features of the underlying contours, a sufficient density of simulations is required, resulting in a process that may be impractical or prohibitively computationally expensive.

To reduce computation time, the principal direction search strategy exploits information concerning the local structure of the basin to conduct a line search in, at most, $2p$ directions, where p is the number of perturbation variables in $\boldsymbol{\mathcal{Y}}$. The principal directions of the perturbation Jacobian, $\frac{\partial \boldsymbol{F}}{\partial \boldsymbol{\mathcal{Y}}}$, are determined by exploiting the eigenvectors of the Cauchy-Green tensor, $\frac{\partial \boldsymbol{F}}{\partial \boldsymbol{\mathcal{Y}}}^T \frac{\partial \boldsymbol{F}}{\partial \boldsymbol{\mathcal{Y}}}$, as evaluated on the reference path.[6] This orthogonal set of vectors corresponds to the local principal stretching directions of the perturbation Jacobian and predicts the local form of the basin. These principal directions are associated with the stretching magnitudes, equivalent to the singular values, σ, of the Jacobian.[7] The benefit of limiting the search to these principal directions in contrast to the naïve

search is illustrated in Figure 2(b), where a finer resolution is achieved with fewer overall simulations by exploiting a search along these principal stretching directions. Unless otherwise noted, basin widths that are estimated for the perturbed targeting problems in this investigation employ the principal direction search method.

In this investigation, basin width associated with a given number of iterations, k_{max}, is determined by bisecting the bounds for the minimum and maximum value of $||\delta \boldsymbol{\mathcal{Y}}_{k_{max}}||$. In the principal direction search strategy, perturbations are modeled as vectors of magnitude s in the direction associated with the principal direction unit vector, $\hat{\boldsymbol{v}}$. The process is initiated with a step of magnitude $s_0 = 10^{-10}$ nondimensional units in the principal direction associated with the maximum stretching direction. The perturbed targeting problem is simulated, and the scale factor s is increased via

$$s_{i+1} = 1.1 s_i$$

until convergence is not achieved within k_{max} targeting iterations. This procedure sets lower and upper bounding values, s_l and s_u, for the basin width corresponding to that principal direction. The next scale factor, s_{i+1}, is then determined by bisecting s_l and s_u. The lower and upper bounding values are updated depending on the perturbed targeting simulations and their convergence characteristics within the iteration limit. The process is terminated when a relative tolerance condition for the scale factor is met, i.e.,

$$\frac{|s_{i+1} - s_i|}{s_{i+1}} < 0.001$$

The final scale factors are determined for each principal direction, in both the positive and negative directions, and the basin width is approximated as the overall minimum scale factor.

Reference Evaluation

In contrast to discretized methods that rely on numerous full simulations of the perturbed targeting problem, previous investigators infer convergence properties in the neighborhood of the baseline solution via the computation of dynamical properties of the baseline solution itself.[2–7] The current effort seeks the correlation between quantities associated with the reference flow and the measured basin width. One such property of the flow is the FTLE, denoted λ_Φ and defined as

$$\lambda_\Phi = \frac{1}{T} \ln(||\Phi||) \tag{4}$$

where $||\cdot||$ is the 2-norm and T is the propagation time associated with the state transition matrix (STM), Φ. The FTLE represents the dominant exponential stretching rate for the volume associated with the STM. In addition to this pure characteristic of the flow, analogous properties are introduced that reflect the coupled nature of the flow and targeting problem formulation, i.e.,

$$\lambda_{\boldsymbol{\mathcal{X}}} = \frac{1}{T} \ln\left(\left|\left|\frac{\partial \boldsymbol{F}}{\partial \boldsymbol{\mathcal{X}}}\right|\right|\right) \tag{5}$$

$$\lambda_{\boldsymbol{\mathcal{Y}}} = \frac{1}{T} \ln\left(\left|\left|\frac{\partial \boldsymbol{F}}{\partial \boldsymbol{\mathcal{Y}}}\right|\right|\right) \tag{6}$$

These 1st-order quantities serve as candidate metrics that may be correlated with the measured basin widths.

A new methodology is also introduced to produce a metric correlated to the basin width. The derivation for this metric originates with an observation regarding the typical evaluation approach for the design variable Jacobian in differential corrections processes. In many applications, the Jacobian in the corrections process is evaluated along the perturbed trajectory rather than the baseline solution. In other words, the design variable Jacobian, $\frac{\partial \boldsymbol{F}}{\partial \boldsymbol{\mathcal{X}}}$, from Equation (3) is updated at each iteration for the current design variables and perturbations $(\boldsymbol{\mathcal{X}}, \boldsymbol{\mathcal{Y}})$ in contrast to fixing the Jacobian at a constant value associated with the baseline, $(\boldsymbol{\mathcal{X}}^*, \boldsymbol{\mathcal{Y}}^*)$. A matrix quantity,

$$\Psi = \left.\frac{\partial \boldsymbol{F}}{\partial \boldsymbol{\mathcal{X}}}\right|^{-1}_{(\boldsymbol{\mathcal{X}}^*, \boldsymbol{\mathcal{Y}}^*)} \left.\frac{\partial \boldsymbol{F}}{\partial \boldsymbol{\mathcal{X}}}\right|_{(\boldsymbol{\mathcal{X}}, \boldsymbol{\mathcal{Y}})} \tag{7}$$

and an associated scalar value,

$$\psi = \max\{\sigma_{\max}(\Psi), \sigma_{\min}(\Psi)^{-1}\} \tag{8}$$

are defined where $\sigma_{\max}$ and $\sigma_{\min}$ denote the maximum and minimum singular values, respectively. These quantities are then employed to conceptualize measures of similarity between the two variational mappings. As the perturbed trajectory is brought arbitrarily close to the baseline, this quantity Ψ approaches the identity matrix, i.e.,

$$\lim_{(\boldsymbol{\mathcal{X}}, \boldsymbol{\mathcal{Y}}) \to (\boldsymbol{\mathcal{X}}^*, \boldsymbol{\mathcal{Y}}^*)} \Psi = I, \qquad \lim_{(\boldsymbol{\mathcal{X}}, \boldsymbol{\mathcal{Y}}) \to (\boldsymbol{\mathcal{X}}^*, \boldsymbol{\mathcal{Y}}^*)} \psi = 1 \tag{9}$$

Through a Taylor series expansion, the design variable Jacobian along the perturbed trajectory is approximated as

$$\left.\frac{\partial \boldsymbol{F}}{\partial \boldsymbol{\mathcal{X}}}\right|_{(\boldsymbol{\mathcal{X}}, \boldsymbol{\mathcal{Y}})} \approx \left.\frac{\partial \boldsymbol{F}}{\partial \boldsymbol{\mathcal{X}}}\right|_{(\boldsymbol{\mathcal{X}}^*, \boldsymbol{\mathcal{Y}}^*)} + \left.\frac{\partial^2 \boldsymbol{F}}{\partial \boldsymbol{\mathcal{X}} \partial \boldsymbol{\mathcal{Y}}}\right|_{(\boldsymbol{\mathcal{X}}^*, \boldsymbol{\mathcal{Y}}^*)} (\delta \boldsymbol{\mathcal{Y}} \otimes I) \tag{10}$$

where $\otimes$ is the Kronecker product. In this formulation, the 2nd -order derivative term is reformatted from a 3-dimensional tensor into a 2-dimensional matrix via

$$\frac{\partial^2 \boldsymbol{F}}{\partial \boldsymbol{\mathcal{X}} \partial \boldsymbol{\mathcal{Y}}} = \begin{bmatrix} \frac{\partial^2 \boldsymbol{F}}{\partial \boldsymbol{\mathcal{X}} \partial \mathcal{Y}_1} & \frac{\partial^2 \boldsymbol{F}}{\partial \boldsymbol{\mathcal{X}} \partial \mathcal{Y}_2} & \cdots & \frac{\partial^2 \boldsymbol{F}}{\partial \boldsymbol{\mathcal{X}} \partial \mathcal{Y}_p} \end{bmatrix} \tag{11}$$

where p is the number of perturbation variables in $\boldsymbol{\mathcal{Y}}$.[14,15] Substituting Equation (10) into the similarity measure in Equation (7) yields

$$\begin{aligned} \Psi &= \left.\frac{\partial \boldsymbol{F}}{\partial \boldsymbol{\mathcal{X}}}\right|^{-1}_{(\boldsymbol{\mathcal{X}}^*, \boldsymbol{\mathcal{Y}}^*)} \left.\frac{\partial \boldsymbol{F}}{\partial \boldsymbol{\mathcal{X}}}\right|_{(\boldsymbol{\mathcal{X}}, \boldsymbol{\mathcal{Y}})} \\ &\approx \left.\frac{\partial \boldsymbol{F}}{\partial \boldsymbol{\mathcal{X}}}\right|^{-1}_{(\boldsymbol{\mathcal{X}}^*, \boldsymbol{\mathcal{Y}}^*)} \left(\left.\frac{\partial \boldsymbol{F}}{\partial \boldsymbol{\mathcal{X}}}\right|_{(\boldsymbol{\mathcal{X}}^*, \boldsymbol{\mathcal{Y}}^*)} + \left.\frac{\partial^2 \boldsymbol{F}}{\partial \boldsymbol{\mathcal{X}} \partial \boldsymbol{\mathcal{Y}}}\right|_{(\boldsymbol{\mathcal{X}}^*, \boldsymbol{\mathcal{Y}}^*)} (\delta \boldsymbol{\mathcal{Y}} \otimes I) \right) \\ &= I + \left.\frac{\partial \boldsymbol{F}}{\partial \boldsymbol{\mathcal{X}}}\right|^{-1}_{(\boldsymbol{\mathcal{X}}^*, \boldsymbol{\mathcal{Y}}^*)} \left.\frac{\partial^2 \boldsymbol{F}}{\partial \boldsymbol{\mathcal{X}} \partial \boldsymbol{\mathcal{Y}}}\right|_{(\boldsymbol{\mathcal{X}}^*, \boldsymbol{\mathcal{Y}}^*)} (\delta \boldsymbol{\mathcal{Y}} \otimes I) \end{aligned} \tag{12}$$

Thus, the deviation of this quantity from identity is denoted the *normalized change in the Jacobian* and is reduced to

$$\Delta\Psi = \frac{\partial \boldsymbol{F}}{\partial \boldsymbol{\mathcal{X}}}^{-1} \frac{\partial^2 \boldsymbol{F}}{\partial \boldsymbol{\mathcal{X}} \partial \boldsymbol{\mathcal{Y}}} (\delta \boldsymbol{\mathcal{Y}} \otimes I)$$

where the matrix quantities are evaluated on the baseline trajectory, i.e., $(\boldsymbol{\mathcal{X}}^*, \boldsymbol{\mathcal{Y}}^*)$. Intuitively, if a large perturbation magnitude and small normalized change in the Jacobian are desirable, the contribution from the expression $\frac{\partial \boldsymbol{F}}{\partial \boldsymbol{\mathcal{X}}}^{-1} \frac{\partial^2 \boldsymbol{F}}{\partial \boldsymbol{\mathcal{X}} \partial \boldsymbol{\mathcal{Y}}}$ should be as small as possible. Therefore, the basin metric, denoted γ, is then defined as

$$\gamma = \left|\left| \frac{\partial \boldsymbol{F}}{\partial \boldsymbol{\mathcal{X}}}^{-1} \frac{\partial^2 \boldsymbol{F}}{\partial \boldsymbol{\mathcal{X}} \partial \boldsymbol{\mathcal{Y}}} \right|\right|^{-1} \tag{13}$$

Basin metric values are expected to positively correlate with the measured values of the basin width.

APPLICATION: L_2 SOUTHERN HALO ORBITS IN THE CRTBP

A suitable sample problem to evaluate the correlation between the numerically measured convergence basin width and the basin metric is introduced as a targeting problem involving the Earth-Moon L2 southern halo family, a family of periodic orbits in the CRTBP — one of particular interest for upcoming space flight missions.[16] A sampling of this periodic orbit family is plotted in Figure 3(a). This family consists of periodic orbits that vary in their proximity to the primary gravitational

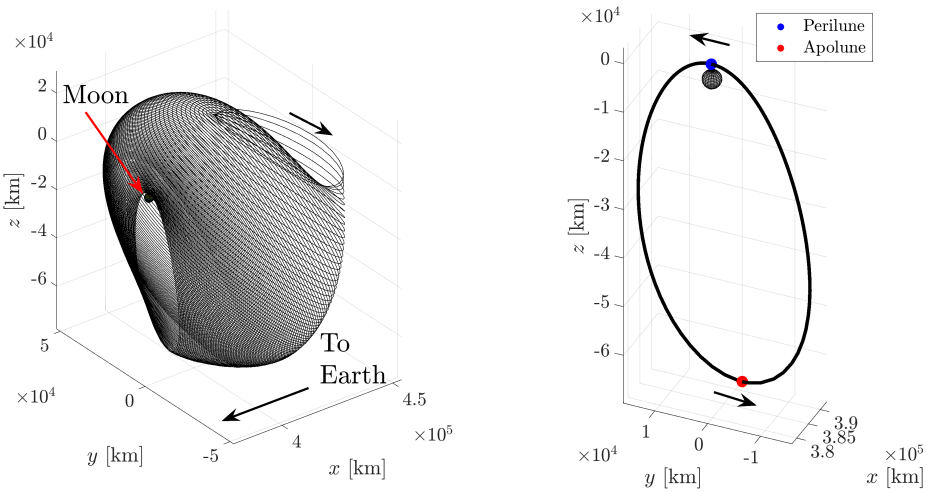

(a) L_2 Southern Halo Family (b) Sample Halo Orbit

Figure 3. L_2 Southern Halo Family in Earth-Moon Rotating Frame

bodies and their stability properties; thus, it is a useful application subset for this analysis. A sample halo orbit is plotted on Figure 3(b) with its perilune and apolune points marked. In this investigation, the L_2 southern halo orbit family is defined from the orbit with perilune distance equal to the lunar radius through the orbit which lies in the $\hat{\boldsymbol{x}}$-$\hat{\boldsymbol{y}}$ plane.

To investigate the convergence basin behavior and the predictive capability of the basin metric, a targeting problem is constructed wherein the position at the initial time is perturbed from the reference. The position after a fixed time-of-flight is constrained, and the initial velocity is varied to target the final position such that it satisfies the constraint. This perturbed targeting problem is represented by

$$\boldsymbol{F} = \boldsymbol{\rho}(t_f) - \boldsymbol{\rho_d} = \boldsymbol{0}, \quad \boldsymbol{\mathcal{X}} = \dot{\boldsymbol{\rho}}(t_0), \quad \boldsymbol{\mathcal{Y}} = \boldsymbol{\rho}(t_0) \tag{14}$$

Recall that $\boldsymbol{\rho}$ is the nondimensional position vector from the barycenter to the spacecraft. For each halo orbit in a sampling of the L_2 southern halo orbits, as distinguished by its unique perilune radius, the initial state is defined at apolune. After a fixed propagation duration, i.e., some integer multiple of the orbit period, the spacecraft is targeted to return to the apolune position.

The principal direction search method is employed to assess the convergence basin width for $k_{max} = 4, \ldots, 8$ iterations. The basin width and basin metric are represented for 1-period, 2-period, and 3-period simulations in Figures 4(a)-4(b), 4(c)-4(d), 4(e)-4(f), respectively. For each perturbed

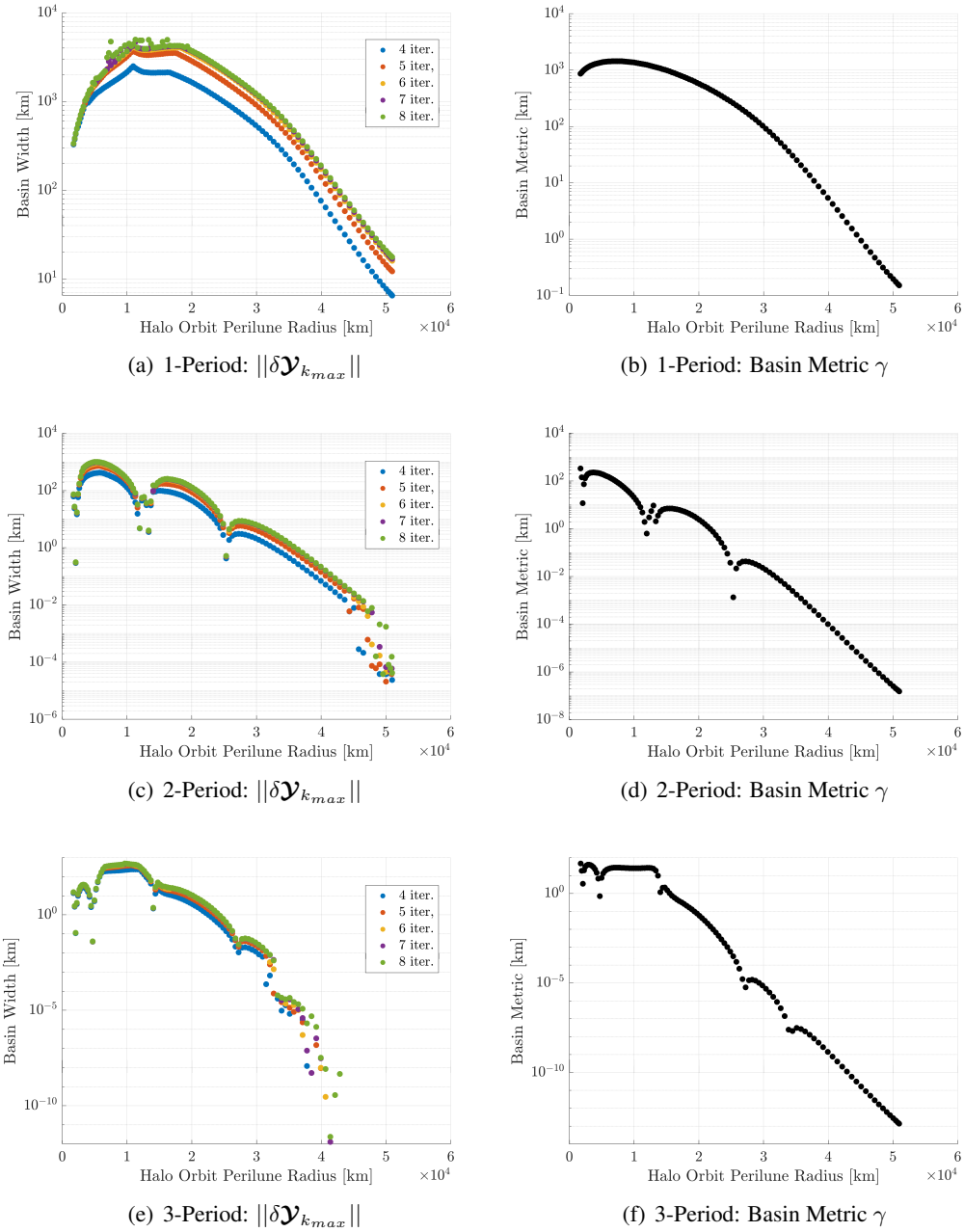

(a) 1-Period: $||\delta\boldsymbol{\mathcal{Y}}_{k_{max}}||$

(b) 1-Period: Basin Metric γ

(c) 2-Period: $||\delta\boldsymbol{\mathcal{Y}}_{k_{max}}||$

(d) 2-Period: Basin Metric γ

(e) 3-Period: $||\delta\boldsymbol{\mathcal{Y}}_{k_{max}}||$

(f) 3-Period: Basin Metric γ

Figure 4. Halo Family Apolune-to-Apolune Targeting

targeting scenario, the basin metric essentially captures the features of the measured basin width. In general, though the magnitudes are different, the forms of the plots of numerically-measured basin width are present in the plots of the computed basin metric. Thus, the basin metric, γ, appears to reliably predict the relative — as opposed to absolute — basin widths of different periodic orbits in the L_2 southern halo family.

Some notable observations from the plots in Figure 4 arise from the numerical aspect of the problem. In general, the relative features of the basin width plots, including slope and critical points, are preserved as the iteration limit, k_{max}, increases from 4 to 8. However, the plots of basin width in Figure 4(a), associated with the 1-period scenario, exhibit scattered and non-smooth behavior for halo orbits with a perilune radius up to approximately 20,000 km when the iteration limit is set to 7 or 8 iterations. This chaotic behavior is indicative of traversal into the chaotic region between main basins in perturbation space and suggests that limits above 6 iterations fail to guarantee convergence to the main convergence basin of the baseline solution. Also on the sample plot for the 1-period scenario, some peaks that represent the basin width occur in Figure 4(a) for orbits with perilune radius between 10,000 and 20,000 km, differing from the relatively smooth basin metric representation in Figure 4(b). The singular values of the perturbation Jacobian $\frac{\partial \boldsymbol{F}}{\partial \boldsymbol{\mathcal{Y}}}$ from the 1-period case are plotted in Figure 5(a). In this plot, the two largest of the three

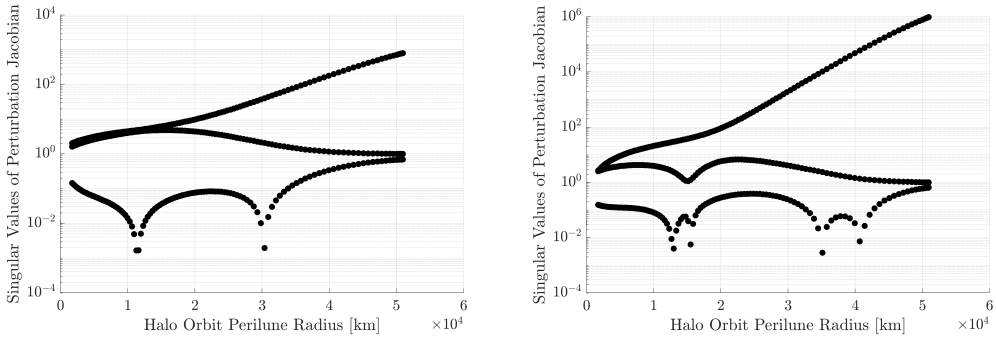

(a) 1-Period (b) 2-Period

Figure 5. Singular Values of Perturbation Jacobian

singular values are nearly equal in magnitude and close to 1 for orbits with a perilune radius of up to 20,000 km. Thus, a single dominant stretching direction is unclear for this subset of the periodic orbit family, and the principal directions associated with these singular values exist in a plane and are not well-defined numerically.[7] Therefore, the actual direction associated with the theoretical basin width may be misaligned in the plane relative to the computed vectors, resulting in some switching behavior that produces the peaks in Figure 4(a). In contrast, the targeting problems with longer propagation times, e.g., the 2-period scenario, possess more distinct singular values, plotted in Figure 5(b), resulting in distinct principal directions with a clear dominant stretching behavior and a basin metric that more accurately captures the numerically-produced width. In Figures 4(c) and 4(e), basin widths for orbits with a large perilune radius are less definitive; the measured basin widths of 1 m or less begin to interact with noise from the numerical convergence and integration tolerances.

The 2-period apolune-to-apolune perturbed targeting problem is selected to further demonstrate the validity of using the principal direction search method as a more efficient approximation of a

broader grid search. For a maximum iteration limit of $k_{max} = 5$, the basin width across the family, as measured via both methods, appears in Figure 6. In general, the measured values of basin width

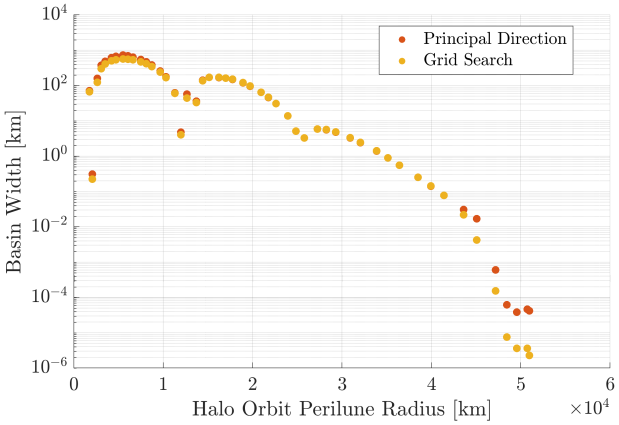

Figure 6. 2-Period: $||\delta \mathcal{Y}_5||$

via the naïve grid search and principal direction search strategies are nearly identical. As perilune radius reaches its maximum value, the difference in measured basin width between the two methods increases. However, this difference occurs when the basin width is on the order of meters, the same order as the numerical tolerances in the targeting problem. Overall, the principal direction search strategy is an efficient and effective substitute for the grid search strategy.

To briefly illustrate the predictive capability of the basin metric, one that relies on 2$^{\text{nd}}$-order state transition tensor information, versus the FTLE-based 1$^{\text{st}}$-order metrics, the 2-period case is selected for comparison. In Figure 7(a), the basin width is plotted across the halo family for the 2-period apolune-to-apolune targeting scenario with $k_{max} = 5$ iterations, and the associated 1$^{\text{st}}$-order FTLE-like metrics are plotted in Figure 7(b). Since the magnitudes of the FTLE-based 1$^{\text{st}}$-order metrics,

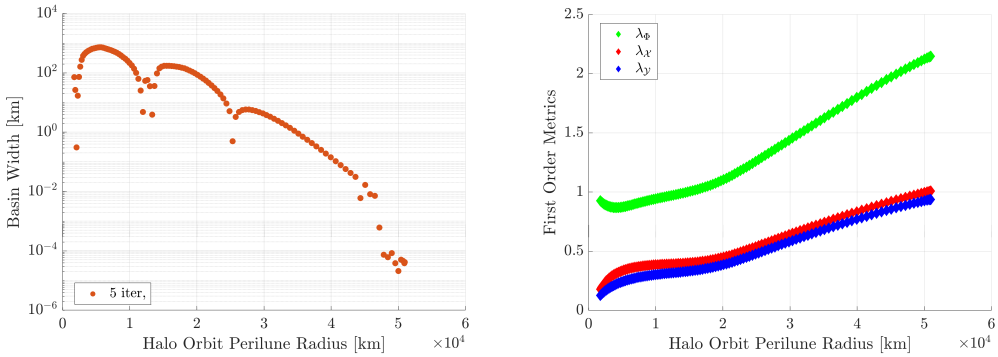

(a) $||\delta \mathcal{Y}_5||$ via Principal Direction Search

(b) FTLE-like First Order Metrics

Figure 7. 2-Period Apolune-to-Apolune Problem

λ_Φ, $\lambda_{\mathcal{X}}$, and $\lambda_{\mathcal{X}}$, correspond to rates of stretching, the basin width is expected to possess a negative correlation to these 1$^{\text{st}}$-order metrics. The increasing trend in FTLE across the family appears to represent the general decreasing trend in basin width, demonstrating the general usefulness in this

quantity as noted in previous investigations. However, the acute basin contractions across the family are not captured by these 1st-order metrics.

A similar perturbed targeting problem is formulated with the final state at the perilune for each member of the L_2 halo orbit family. Analogous to the apolune-to-apolune examples, these apolune-to-perilune problems are simulated for 1.5-period, 2.5-period, and 3.5-period times-of-flight, and the results appear in Figures 8(a)-8(b), 8(c)-8(d), and 8(e)-8(f), respectively. Again, the qualitative

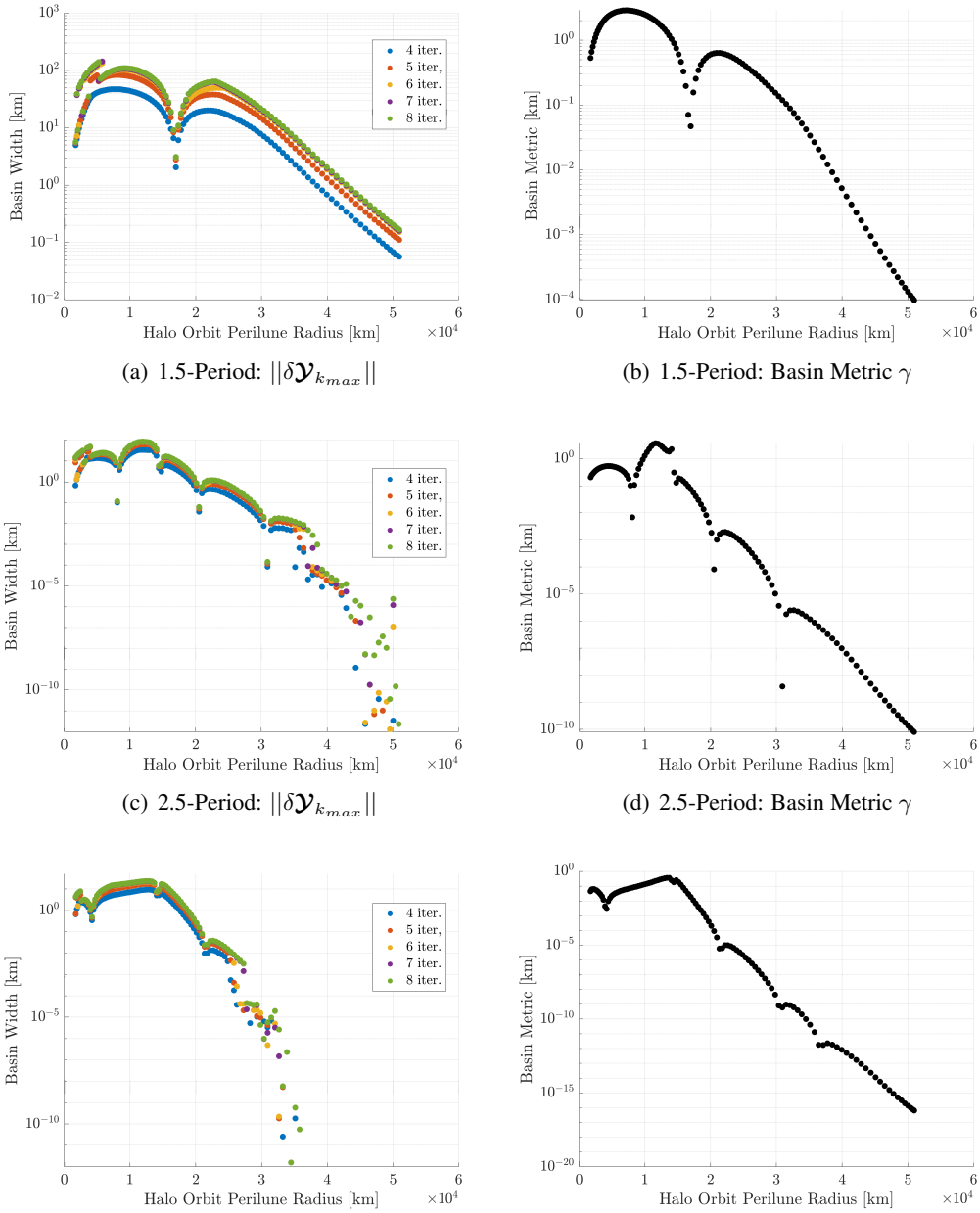

(a) 1.5-Period: $||\delta \boldsymbol{\mathcal{Y}}_{k_{max}}||$

(b) 1.5-Period: Basin Metric γ

(c) 2.5-Period: $||\delta \boldsymbol{\mathcal{Y}}_{k_{max}}||$

(d) 2.5-Period: Basin Metric γ

(e) 3.5-Period: $||\delta \boldsymbol{\mathcal{Y}}_{k_{max}}||$

(f) 3.5-Period: Basin Metric γ

Figure 8. Halo Family Apolune-to-Perilune Targeting

features of the basin width plots are represented in the corresponding values of the basin metric, γ. Similar to the apolune-to-apolune targeting scenarios, the interaction of the basin width and the numerical tolerances of the problem produces scattered behavior for orbits with a large perilune radius, and this trend becomes more pronounced as longer propagation times induce smaller basin widths. Additionally, basin width appears irregular and discontinuous for orbits with a small perilune radius, as it appears in Figure 8(a) for perilune radii of up to approximately 5,000 km, suggesting traversal into the chaotic region between main convergence basins. For the purpose of highlighting where the constrictions in the convergence basin occur across the family, the simply-evaluated basin metric is sufficient to approximate the simulation-heavy measured results.

APPLICATION: HIGHER FIDELITY L_1-TO-L_2 TRANSIT

To explore the correlation of the predictive basin metric and the numerically-produced basin width in a different dynamical regime, a transfer trajectory is constructed in the Sun-Earth system. The Genesis mission, depicted in Figure 9, reproduced from NASA's mission website,[17] entered into an L_1 halo orbit in the Sun-Earth system to collect solar wind samples before leveraging dynamics near the L_2 point to return to Earth.[18] Represented in the Sun-Earth rotating frame as a dashed

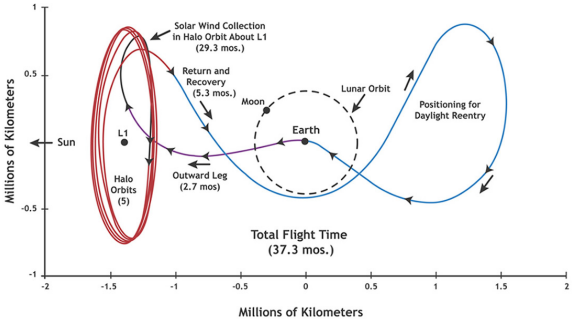

Figure 9. Genesis Mission Trajectory

orange line in Figure 10, a trajectory, based on work in support of the Genesis mission,[19] is corrected to be continuous in position and velocity in an ephemeris force model, consisting of the Sun, Earth, and Moon. A portion of this trajectory, colored in blue in Figure 10, represents the departure

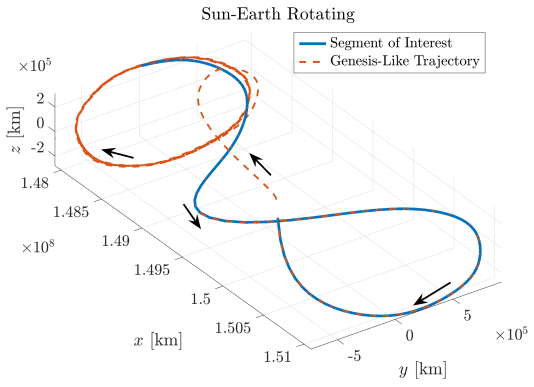

Figure 10. Genesis-like Trajectory with L_1-to-L_2 Transit of Interest

from the L_1 halo orbit, transit to the L_2 vicinity, and return to the Earth vicinity. This final leg of the mission, traversing the L_1 and L_2 vicinities with a close pass of the Earth, serves as the baseline solution and the focus of this convergence basin analysis. The perturbed targeting problem associated with this baseline trajectory is formulated with

$$\boldsymbol{F} = \boldsymbol{r}_{ESc}(t_f) - \boldsymbol{r}_{ESc,d} = \boldsymbol{0}, \quad \boldsymbol{\mathcal{X}} = \dot{\boldsymbol{r}}_{ESc}(t_0), \quad \boldsymbol{\mathcal{Y}} = \boldsymbol{r}_{ESc}(t_0) \tag{15}$$

where $\boldsymbol{r}_{ESc}$ is the position from the Earth (E) to the spacecraft (Sc) in the J2000 reference frame. Two characterizations of the convergence basin are performed: (*i*) as the spacecraft moves downstream along the trajectory and (*ii*) as the initial epoch is offset over the course of 28 days. These applications reflect typical analyses that may be of interest to mission designers.

Convergence Basins Along the Baseline Trajectory

Knowledge of the convergence basin characteristics along a baseline trajectory allows mission designers to determine times when re-targeting to account for accumulated errors is more or less likely to converge on a feasible solution. To analyze the convergence basin along the baseline trajectory, the principal direction search method is used to measure the basin width at different points in time as the spacecraft moves downstream along the baseline trajectory. The targeting epoch, t_0, is the time at which the perturbation is applied and targeting is simulated, and this analysis is conducted as t_0 moves between the initial and final epochs of the full baseline trajectory, $t_{0,ref}$ and t_f, respectively. The numerically-measured basin width, defined for the iteration limit of 20 iterations, is plotted in Figure 11(a). In this plot, time is measured as the difference between t_0 and

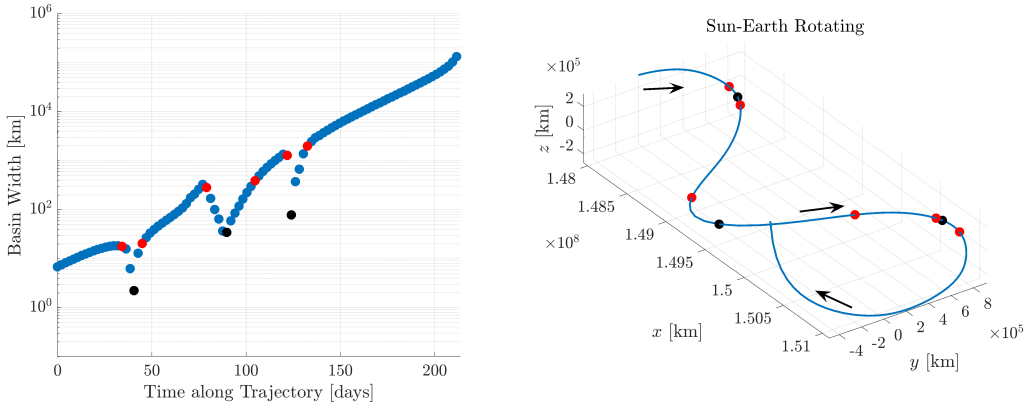

(a) Convergence Basin Wells (b) Baseline Trajectory

Figure 11. Locations Along Baseline Trajectory with Constricted Convergence Basins

$t_{0,ref}$, reflecting the time along the trajectory since the last perilune of the L_1 halo orbit. As the targeting epoch is brought closer to the final time, in general, the basin width possesses a general positive trend, punctuated by local minima and maxima. The local minima in basin width, marked in black, occur along the trajectory and accompany regions of basin constriction, marked on either side by a red point. The corresponding locations along the trajectory are marked in Figure 11(b). Though the second local minimum, associated a close approach of the Earth-Moon vicinity, is commonly identified as a sensitive region, the existence of the first and third local minima may not fit within the intuition of a mission designer. Thus, the ability to predict these minima without running large batches of targeting simulations is valuable.

Applying the basin metric methodology to this perturbed targeting problem yields a useful correlative surrogate to the basin width. Plotted in Figure 12 alongside the measured basin width, the basin metric calculated at each targeting time, t_0, captures the relative behavior of the basin width as the targeting time is moved downstream. Though the magnitudes differ, the three local minima

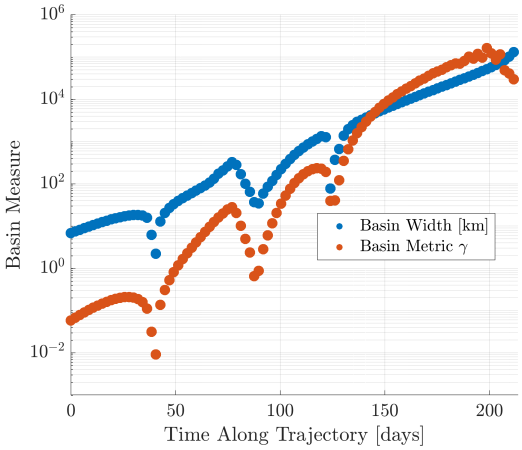

Figure 12. Basin Width vs. Metric for Varied Targeting Time

are present in each plot and occur at the same times along the baseline trajectory. The information captured by the basin metric may be useful in determining how to place trajectory correction maneuvers ahead of convergence basin contractions. This basin metric, requiring only information associated with the baseline trajectory, may be stored on-board spacecraft for automated determination of correction maneuver times.

Convergence Basins with Varying Departure Epochs

Another possible mission design task is to assess changes in the targeting feasibility for new baseline trajectories generated by varying the launch epoch. To simulate this task, new baseline trajectories are produced by shifting the initial epoch of the entire original baseline trajectory, shown in Figure 10, in single day increments over the course of 28 days, chosen to capture the effects of lunar phasing. The original baseline trajectory, plotted in Figure 10, is conceived as possessing a +0 day epoch shift. To preserve the basic geometry of the transfer in configuration space, this original baseline trajectory is discretized into a series of patch point nodes and then re-targeted at each new epoch to achieve state and epoch continuity using a multiple-shooting targeter within the ATD software package. This process results in 28 new baseline trajectories that have a similar geometry but reflect changes in the positioning and orientation of the gravitational bodies. A sampling of these trajectories is plotted in Figure 13 for epoch shifts of +0, +7, +14, +21, and +28 days. The effects of the different positions of the gravitational bodies at each starting epoch are apparent in the drift in baseline trajectories; however, the overall geometry of the original baseline is successfully preserved.

The perturbed targeting problem outlined in Equation (15) is employed, where the final desired position is the final position uniquely associated with each epoch-shifted baseline trajectory. For each baseline trajectory across the 28 day survey, the basin width, measured via numerous targeting simulations within the principal direction search strategy, and the basin metric, computed via state

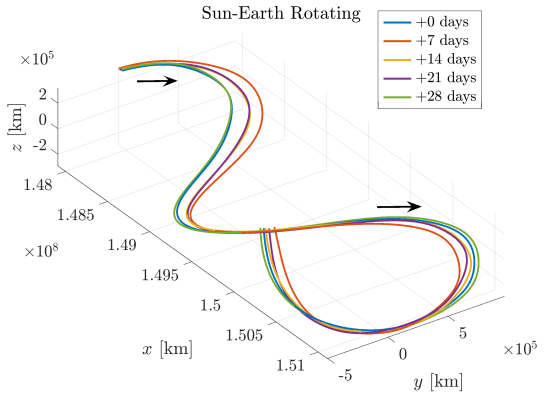

Figure 13. Sampling of Epoch-Shifted Baseline Trajectories

transition tensors for each baseline, are plotted in Figure 14. Again, the relative features present

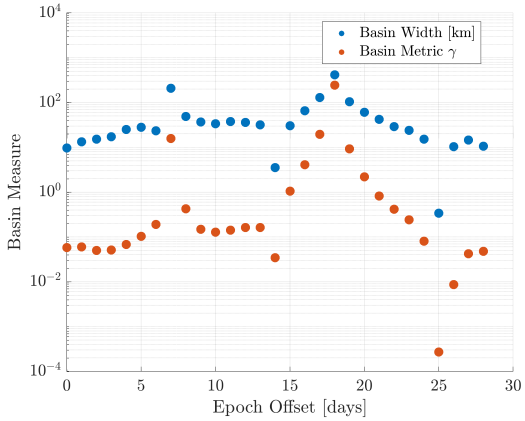

Figure 14. Basin Width vs. Basin Metric for Epoch-Shifted Baselines

in the basin metric for each epoch-shifted trajectory mirror the features seen in the measured basin width. All expansions and contractions of the basin width as the trajectory is offset in epoch are represented in the basin metric. Local maxima in both basin width and basin metric occur for the +7 and +18 day offset baseline trajectories, communicating that relatively large perturbations may be accommodated. For the +14 and +25 day baseline scenarios, local minima occur in each basin quantity, highlighting that targeting in the vicinity of these baseline solutions is especially sensitive to perturbations.

CONCLUDING REMARKS

In space flight, foreknowledge of the convergence behavior along a pre-planned baseline trajectory is critical to mission success. Traditional techniques to assess the ability of a targeting strategy to correct for perturbations to a baseline trajectory, such as Monte Carlo simulations, contribute a

substantial portion to the computational and scheduling requirements of the verification and validation stage of a mission. Additionally, the effectiveness of these discretization-based methods is contingent on the proper refinement of points, which may require multiple attempts and numerous simulations. To more efficiently quantify and characterize convergence behavior of a baseline solution, this work introduces a framework for defining the width of a convergence basin and proposes the principal direction search method as a means of reducing the computational cost of numerically measuring the basin. By combining information about the dynamical properties of the baseline trajectory and the formulation of the targeting problem, this work then derives a metric associated with the baseline itself and investigates the correlation of this metric to the numerically-measured basin widths for trajectories within two different force models and regions of space.

In general, the behavior of the 2^{nd}-order basin metric, γ, correlates strongly with the behavior of the measured basin width. Though the basin metric does not directly predict the value of the perturbation magnitude associated with the basin width, a relative assessment of the basin metrics for a given set of baseline trajectories reflects the relative basin widths of these baselines. Since the 1^{st}-order metrics analyzed in this investigation, such as the FTLE, are demonstrated to be insufficient for predicting the major features of the convergence basin, a natural question arises about whether metrics with information of orders higher than 2 may be beneficial. For the applications examined in this investigation, there appears to be no additional benefit to exploring 3^{rd}-order metrics, because the plots of the 2^{nd}-order basin metric, γ, capture the key features in the measured basin width plots. The predictive measure of the convergence basin metric derived and introduced in this work lays a foundation for methods to identify the relative convergence properties of design options, diagnose convergence difficulties in existing designs, and model convergence behavior for onboard maneuver planning.

ACKNOWLEDGEMENTS

The authors thank NASA Johnson Space Center (JSC) and Purdue University School of Aeronautics and Astronautics for facilities and support. The authors would also like to thank the members of the Multibody Dynamics Research Group at Purdue University. Portions of this work were completed in collaboration with NASA JSC and at Purdue University through Grant NASA JSC 80NSSC19K1175.

REFERENCES

[1] M. G. Epitropakis and M. N. Vrahatis, "Studying the Basin of Convergence of Methods for Computing Periodic Orbits," *International Journal of Bifurcation and Chaos*, Vol. 21, No. 8, 2011, pp. 2079–2106.

[2] G. Harden, A. Haapala, K. C. Howell, and B. Marchand, "Automated Patch Point Placement for Spacecraft Trajectory Targeting," *AAS/AIAA Space Flight Mechanics Meeting*, Santa Fe, New Mexico, January 26-30, 2014.

[3] C. Spreen, *Automated Patch Point Placement Capability for Hybrid Trajectory Targeting*. PhD dissertation, Purdue University, West Lafayette, Indiana, December 2017.

[4] C. Spreen and K. C. Howell, "Automated Node Placement Capability for Spacecraft Trajectory Targeting Using Higher-Order State Transition Matrices," *AAS/AIAA Astrodynamics Specialists Conference*, Columbia River Gorge, Stevenson, Washington, August 21-24, 2017.

[5] C. E. York and K. C. Howell, "A Two-Level Differential Corrections Algorithm for Low-Thrust Spacecraft Trajectory Targeting," *29th AAS/AIAA Space Flight Mechanics Meeting*, Ka'anapali, Maui, Hawaii, January 13-17, 2019.

[6] V. Muralidharan and K. C. Howell, "Orbit Maintenance Strategy for Earth-Moon Halo Orbits," *31st AAS/AIAA Spaceflight Mechanics Meeting*, Charlotte, North Carolina, February 1 - 3, 2021.

[7] V. Muralidharan, *Stretching Directions in Cislunar Space: Stationkeeping and an Application to Transfer Trajectory Design*. PhD dissertation, Purdue University, West Lafayette, Indiana, August 2021.

[8] T. F. Dawn, J. P. Gutkowski, A. L. Batcha, and S. M. Pedrotty, "Trajectory Design Considerations for Exploration Mission 1," *AAS/AIAA Space Flight Mechanics Meeting*, Kissimee, Florida, January, 2018.

[9] A. L. Batcha *et al.*, "Artemis I Trajectory Design and Optimization," *AAS/AIAA Astrodynamics Specialist Conference*, Virtual, August 9-12, 2020.

[10] V. Szebehely, *Theory of Orbits: The Restricted Problem of Three Bodies*. New York and London: Academic Press, 1967.

[11] D. Guzzetti, N. Bosanac, D. Folta, and K. Howell, "A Framework for Efficient Trajectory Comparisons in the Earth-Moon Design Space," *AAS/AIAA Astrodynamics Specialist Conference*, San Diego, California, August, 2014.

[12] M. Hintermuller, "Semismooth Newton Methods and Applications," Oberwolfach-Seminar on "Mathematics of PDE-Constrainted Optimization" at Mathematisches Forschungsinstitut in Oberwolfach, November, 2010.

[13] J. F. Epperson, *An Introduction to Numerical Methods and Analysis*. New York: J. Wiley, 2 ed., 2002.

[14] M. Majji, J. L. Junkins, and J. D. Turner, "A higher order method for estimation in dynamic systems," *Journal of the Astronautical Sciences*, Vol. 56, No. 3, 2008, p. 401.

[15] J. L. Junkins, M. Majji, and J. D. Turner, "High Order Keplerian State Transition Tensors," *Proceedings of the F. Landis Markley Astronautics Symposium*, Cambridge, Maryland, 2008, pp. 169–186.

[16] E. M. Zimovan, K. C. Howell, and D. C. Davis, "Near Rectilinear Halo Orbits and Their Application in Cis-Lunar Space," *3rd Academy of Astronautics Conference on Dynamics and Control of Space Systems*, Moscow, Russia, May 30 - June 1, 2017.

[17] NASA, "Genesis Mission Trajectory and Flight Plan," Nov 2009. https://solarsystem.nasa.gov/genesismission/gm2/images/gallery/artist_renderings/artist_renderings9.htm.

[18] M. Lo *et al.*, "GENESIS Mission Design," *Journal of Astronautical Sciences*, Vol. 49, January-March 2001, pp. 107–125.

[19] B. Barden, R. Wilson, K. C. Howell, and B. Marchand, "Summer Launch Options for the Genesis Mission," *AAS/AIAA Astrodynamics Specialists Conference*, Quebec City, Canada, July 30 - August 2, 2001.